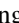


















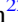














HD 202772A b: A Transiting Hot Jupiter around a Bright, Mildly Evolved Star in a Visual Binary Discovered by *TESS*

Songhu Wang^{1,34} , Matias Jones², Avi Shporer³ , Benjamin J. Fulton^{4,5} , Leonardo A. Paredes⁶, Trifon Trifonov⁷ , Diana Kossakowski⁷, Jason Eastman⁸ , Seth Redfield⁹ , Maximilian N. Günther^{3,35} , Laura Kreidberg^{8,10} , Chelsea X. Huang^{3,35} , Sarah Millholland^{1,36} , Darryl Seligman¹, Debra Fischer¹ , Rafael Brahm^{11,12,13} , Xian-Yu Wang^{14,15}, Bryndis Cruz¹, Todd Henry¹⁶, Hodari-Sadiki James⁶, Brett Addison¹⁷, En-Si Liang¹⁸, Allen B. Davis¹ , René Tronsgaard¹⁹, Keduse Worku¹, John M. Brewer¹ , Martin Kürster⁷, Hui Zhang¹⁸ , Charles A. Beichman⁵, Allyson Bieryla⁸ , Timothy M. Brown^{20,21} , Jessie L. Christiansen⁵ , David R. Ciardi⁵, Karen A. Collins⁸ , Gilbert A. Esquerdo⁸, Andrew W. Howard⁴, Howard Isaacson²² , David W. Latham⁸ , Tsevi Mazeh²³, Erik A. Petigura⁴, Samuel N. Quinn⁸ , Sahar Shahaf²³, Robert J. Siverd²⁴ , Florian Rodler²⁵, Sabine Reffert²⁶, Olga Zakhozhay^{7,27}, George R. Ricker³, Roland Vanderspek³ , Sara Seager^{3,28}, Joshua N. Winn²⁹ , Jon M. Jenkins³⁰ , Patricia T. Boyd³¹ , Gábor Fűrész³, Christopher Henze³⁰, ALEN M. LEVINE³, Robert Morris³², Martin Paegert⁸ , Keivan G. Stassun^{24,33} ,

Eric B. Ting³⁰, Michael Vezie³, and Gregory Laughlin¹ 

¹ Department of Astronomy, Yale University, New Haven, CT 06511, USA; song-hu.wang@yale.edu

² European Southern Observatory, Casilla 19001, Santiago, Chile

³ Department of Physics and Kavli Institute for Astrophysics and Space Research, Massachusetts Institute of Technology, Cambridge, MA 02139, USA

⁴ California Institute of Technology, Pasadena, CA 91125, USA

⁵ IPAC-NASA Exoplanet Science Institute Pasadena, CA 91125, USA

⁶ Physics and Astronomy Department, Georgia State University, Atlanta, GA 30302, USA

⁷ Max-Planck-Institut für Astronomie, Königstuhl 17, D-69117 Heidelberg, Germany

⁸ Harvard-Smithsonian Center for Astrophysics, 60 Garden Street, Cambridge, MA 02138, USA

⁹ Astronomy Department and Van Vleck Observatory, Wesleyan University, Middletown, CT 06459, USA

¹⁰ Harvard Society of Fellows, 78 Mount Auburn Street, Cambridge, MA 02138, USA

¹¹ Center of Astro-Engineering UC, Pontificia Universidad Católica de Chile, Av. Vicuña Mackenna 4860, 7820436 Macul, Santiago, Chile

¹² Instituto de Astrofísica, Pontificia Universidad Católica de Chile, Av. Vicuña Mackenna 4860, Macul, Santiago, Chile

¹³ Millennium Institute for Astrophysics, Chile

¹⁴ Key Laboratory of Optical Astronomy, National Astronomical Observatories, Chinese Academy of Sciences, Beijing 100012, People's Republic of China

¹⁵ University of Chinese Academy of Sciences, Beijing, 100049, People's Republic of China

¹⁶ RECONS Institute, Chambersburg, PA, USA

¹⁷ University of Southern Queensland, Toowoomba, Qld 4350, Australia

¹⁸ School of Astronomy and Space Science & Key Laboratory of Modern Astronomy and Astrophysics in Ministry of Education, Nanjing University, Nanjing 210023, People's Republic of China

¹⁹ DTU Space, National Space Institute, Technical University of Denmark, Elektrovej 328, DK-2800 Kgs. Lyngby, Denmark

²⁰ Las Cumbres Observatory, 6740 Cortona Dr., Suite 102, Goleta, CA 93117, USA

²¹ University of Colorado/CASA, Boulder, CO 80309, USA

²² Astronomy Department, University of California, Berkeley, CA 94720, USA

²³ School of Physics and Astronomy, Tel Aviv University, Tel Aviv 69978, Israel

²⁴ Department of Physics and Astronomy, Vanderbilt University, Nashville, TN 37235, USA

²⁵ European Southern Observatory (ESO), Alonso de Cordova 3107, Vitacura, Santiago de Chile, Chile

²⁶ Landessternwarte, Zentrum für Astronomie der Universität Heidelberg, Königstuhl 12, D-69117 Heidelberg, Germany

²⁷ Main Astronomical Observatory, National Academy of Sciences of the Ukraine, 03143 Kyiv, Ukraine

²⁸ Earth and Planetary Sciences, MIT, 77 Massachusetts Avenue, Cambridge, MA 02139, USA

²⁹ Department of Astrophysical Sciences, Princeton University, 4 Ivy Lane, Princeton, NJ 08544, USA

³⁰ NASA Ames Research Center, Moffett Field, CA 94035, USA

³¹ NASA Goddard Space Flight Center, 8800 Greenbelt Road, Greenbelt, MD 20771, USA

³² SETI Institute, 189 Bernardo Avenue, Suite 200, Mountain View, CA 94043, USA

³³ Department of Physics, Fisk University, Nashville, TN 37208, USA

Received 2018 October 3; revised 2018 November 13; accepted 2018 November 16; published 2019 January 14

Abstract

We report the first confirmation of a hot Jupiter discovered by the *Transiting Exoplanet Survey Satellite* (*TESS*) mission: HD 202772A b. The transit signal was detected in the data from *TESS* Sector 1, and was confirmed to be of planetary origin through radial velocity (RV) measurements. HD 202772A b is orbiting a mildly evolved star with a period of 3.3 days. With an apparent magnitude of $V = 8.3$, the star is among the brightest and most massive known to host a hot Jupiter. Based on the 27 days of *TESS* photometry and RV data from the CHIRON, HARPS, and Tillinghast Reflector Echelle Spectrograph, the planet has a mass of $1.017^{+0.070}_{-0.068} M_J$ and radius of $1.545^{+0.052}_{-0.060} R_J$, making it an inflated gas giant. HD 202772A b is a rare example of a transiting hot Jupiter around a quickly evolving star. It is also one of the most strongly irradiated hot Jupiters currently known.

Key words: planetary systems – planets and satellites: detection – stars: individual (TIC 290131778-TOI 123-HD 202772 – techniques: radial velocities

³⁴ 51 Pegasi b Fellow.

³⁵ Juan Carlos Torres Fellow.

³⁶ NSF Graduate Research Fellow.

1. Introduction

Hot Jupiters, owing to their ease of detectability, constitute the best-studied population of extrasolar planets. However, we still do not understand how these behemoths came into existence. Did they form in situ (Bodenheimer et al. 2000; Batygin et al. 2016), or did they arise in wider orbits and migrate to their current locations (Lin et al. 1996)? If hot Jupiters did undergo migration, was this process violent (Rasio & Ford 1996; Wu et al. 2007; Wu & Lithwick 2011; Petrovich 2015) or quiescent (Lin et al. 1996)? Are the highly inclined and eccentric orbits of some hot Jupiters a consequence of high-eccentricity migration (Winn et al. 2010; Bonomo et al. 2017) or other mechanisms that are unrelated to planet migration (Duffell & Chiang 2015; Lai 2016)? What is the occurrence rate of hot Jupiters as a function of stellar age (Donati et al. 2016)? What is the meaning of the high rate of distant companions (Knutson et al. 2014) and the low rate of close-in companions (Becker et al. 2015) to hot Jupiters? What are the connections between hot Jupiters and warm Jupiters (Huang et al. 2016), hot Neptunes (Dong et al. 2018), compact multiple-planet systems (Lee & Chiang 2016), and ultra-short-period planets (Winn et al. 2018)? These questions may be easier to answer if we enlarge the sample of hot Jupiters around very bright stars, subject to a wide range of irradiation levels.

The recently commissioned *Transiting Exoplanet Survey Satellite* (*TESS*; Ricker et al. 2015) mission has the main goal of discovering transiting exoplanets around bright and nearby stars, thereby facilitating follow-up studies. A few dozen hot Jupiters orbiting bright ($V \lesssim 10$ mag) stars are expected to emerge from the *TESS* mission (Sullivan et al. 2015; Barclay et al. 2018; Huang et al. 2018). They will always be among the most observationally favorable transiting planets, and as such, they will be observed in perpetuity as astronomical capabilities advance.

Here we report the first confirmation of a hot Jupiter discovered by the *TESS* mission, HD 202772A b. Section 2 presents the data. Section 3 describes the derivation of the host star characteristics, and Section 4 presents the system parameters based on fitting the available photometry and RV data. Section 5 summarizes the results and places this discovery into context.

2. Observation and Data Reduction

2.1. *TESS* Photometry

HD 202772 (TIC 290131778, TOI 123) was observed by Camera 1 of the *TESS* spacecraft during the first sector of science operations, between 2018 July 25 and 2018 August 22 (BJD 2458325 to 2458353). The available data have two-minute time sampling (“short cadence”). Some basic parameters of the target are given in Table 1. Given its position in the sky, HD 202772 will not be re-observed during the *TESS* primary mission. The photometric data were analyzed by the Science Processing Operations Center (SPOC) pipeline, based on the NASA *Kepler* mission pipeline (J. Jenkins et al. 2018, in preparation). The light curve of HD 202772 presented in Figure 1 shows a clear transit signal. It was listed among the *TESS* Alerts published online on 2018 September 5, prompting us to download the photometric time series.³⁷

We detrended the raw light curves in the following way (see, e.g., Günther et al. 2017, 2018). After masking out all of the data obtained during transits, we fitted a Gaussian Process (GP) model to the data, using a Matern 3/2 kernel and a white noise kernel. For this task, we employed the CELERITE package, which uses a Taylor-series expansion of these kernel functions. Once the parameters of the GP were constrained based on the out-of-transit data, we used it to detrend the entire light curve.

The SPOC pipeline produces flags for poor-quality exposures. These include exposures taken during the 30-minute momentum dumps that occurred every 2.5 days (10 times in total). All flagged exposures were omitted from our analysis. The resulting light curve is plotted in Figure 1.

2.2. Keck/NIRC2 Adaptive Optics (AO) Imaging

HD 202772 was reported to be a pair of stars separated by $\approx 1.5''$ in several wide-field surveys (e.g., Tycho-2, Høg et al. 2000; PPMXL, Roeser et al. 2010; *Gaia* DR2, *Gaia* Collaboration et al. 2018; see also Holden 1978; Horch et al. 2001), although the *Gaia* DR2 catalog flags the brighter star as a “duplicate” entry. To check on these earlier findings, we performed high-resolution AO imaging at Keck Observatory.

The Keck observations were made with the NIRC2 instrument on Keck II behind the natural guide star AO system. The observations were made on 2018 September 18 on a night with partial cirrus conditions. We used the standard 3-point dither pattern that avoids the left lower quadrant of the detector (which is typically noisier than the other three quadrants). The dither pattern step size was $3''$, and it was repeated twice, with the second dither offset from the first dither by $0''.5$. Observations were made with three different filters: narrow-band Br_γ ($\lambda_o = 2.1686$; $\Delta\lambda = 0.0326 \mu\text{m}$), H -continuum ($\lambda_o = 1.5804$; $\Delta\lambda = 0.0232 \mu\text{m}$), and J -continuum ($\lambda_o = 1.2132$; $\Delta\lambda = 0.0198 \mu\text{m}$), using integration times of 1.45, 5.0, and 1.5 s, respectively. The camera was in the narrow-angle mode with a full field of view of $10''$ and a pixel scale of approximately $0''.01$ per pixel.

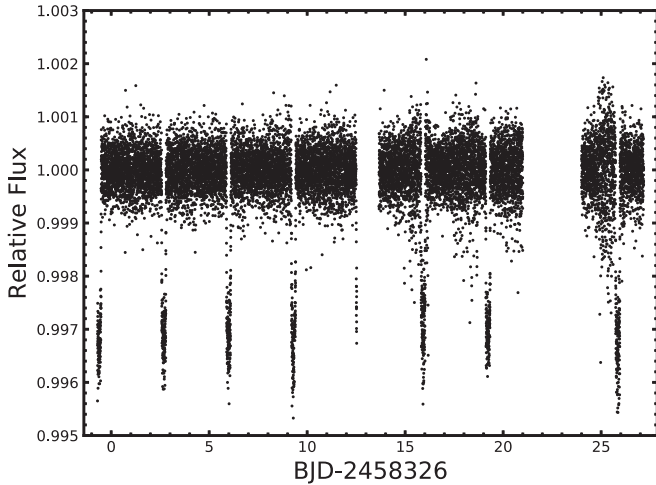
Two stars were clearly detected, with a separation of $1''.3$ (Figure 2). The resolution of the $2 \mu\text{m}$ image is approximately $0''.05$ FWHM. The sensitivity of the final combined AO image was determined by injecting simulated sources azimuthally around the primary target every 45° at separations of integer multiples of the FWHM of the central source (Furlan et al. 2017). The brightness of each injected source was scaled until standard aperture photometry detected it with 5σ significance. The resulting brightness of the injected sources relative to our target was taken to be the contrast limit for the injected location. The final 5σ limit at each separation was determined from the average of all of the determined limits at that separation, with an uncertainty given by the rms dispersion of the results for different azimuthal slices. Figure 2 shows the $2 \mu\text{m}$ sensitivity curve in black, with the 1σ (rms) dispersion marked in purple. The inset image shows the primary target in the center and the second source located $1''.3$ to the northwest.

The two stars were detected in all three filters. The presence of the blended companion must be taken into account to obtain the correct transit depth and planetary radius (Ciardi et al. 2015). The stars have blended 2MASS magnitudes of $J = 7.232 \pm 0.026$ mag, $H = 7.048 \pm 0.021$ mag, and $K_s = 6.945 \pm 0.026$ mag. The stars have measured magnitude differences of $\Delta J = 1.705 \pm$

³⁷ The Alerts and data products from *TESS* Sector 1 are publicly available from NASA’s Mikulski Archive for Space Telescopes (MAST).

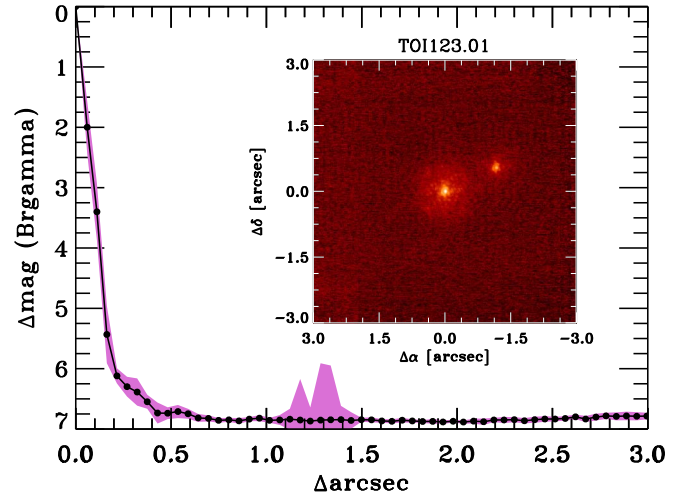
Table 1
HD 202772

Parameter	HD 202772A	HD 202772B	Source
R.A. (hh:mm:ss)	21:18:47.901	21:18:47.813	<i>Gaia</i> DR2
Decl. (dd:mm:ss)	-26:36:58.95	-26:36:58.42	<i>Gaia</i> DR2
μ_α (mas yr ⁻¹)	28.360 ± 0.269	23.236 ± 0.157	<i>Gaia</i> DR2
μ_δ (mas yr ⁻¹)	-56.533 ± 0.418	-57.557 ± 0.152	<i>Gaia</i> DR2
Parallax (mas)	6.166 ± 0.092	6.686 ± 0.109	<i>Gaia</i> DR2
<i>B</i> (mag)	8.81 ± 0.02	10.65 ± 0.02	Tycho
<i>V</i> (mag)	8.320 ± 0.05	10.15 ± 0.05	Tycho
<i>TESS</i> (mag)	7.92 ± 0.09	9.62 ± 0.09	TIC V7 ^a
<i>J</i> (mag)	7.437 ± 0.027	9.142 ± 0.029	NIRC2; this paper
<i>H</i> (mag)	7.266 ± 0.021	8.897 ± 0.022	NIRC2; this paper
<i>K_s</i> (mag)	7.149 ± 0.017	8.858 ± 0.018	NIRC2; this paper
<i>Spectroscopic and Derived Properties</i>			
<i>T</i> _{eff} (K)	6330 ± 100	6156 ± 100	Keck/HIRES; this paper
log <i>g</i> _* (cgs)	4.03 ± 0.10	4.24 ± 0.10	Keck/HIRES; this paper
[Fe/H] (dex)	0.29 ± 0.06	0.25 ± 0.06	Keck/HIRES; this paper
<i>M</i> _* (<i>M</i> _⊙)	1.69 ^{+0.05} _{-0.04}	1.21 ± 0.04	Keck/HIRES; this paper
<i>R</i> _* (<i>R</i> _⊙)	2.515 ^{+0.137} _{-0.127}	1.16 ± 0.06	Keck/HIRES; this paper
Age (age)	1.52 ^{+0.19} _{-0.20}	1.27 ^{+1.32} _{-0.80}	Keck/HIRES; this paper

Note.^a Stassun et al. (2018).**Figure 1.** The *TESS* Sector 1 light curve of HD 202772A, with two-minute cadence. Instrumental signals have already been removed from these data. The periodic decreases in flux are the transits of HD 202772A b. The gap in the middle of the light curve is due to the data download, which was performed at the end of the satellite’s ninth orbit.

0.0015 mag, $\Delta H = 1.631 \pm 0.008$ mag, and $\Delta K_s = 1.709 \pm 0.011$ mag. The primary star has deblended apparent magnitudes of $J_1 = 7.437 \pm 0.027$ mag, $H_1 = 7.266 \pm 0.021$ mag, and $K_{s1} = 7.149 \pm 0.017$ mag, corresponding to $(J - H)_1 = 0.171 \pm 0.034$ mag and $(H - K_s)_1 = 0.117 \pm 0.027$ mag. The secondary star has deblended apparent magnitudes of $J_2 = 9.142 \pm 0.029$ mag, $H_2 = 8.897 \pm 0.022$ mag, and $K_{s2} = 8.858 \pm 0.018$ mag, corresponding to $(J - H)_2 = 0.245 \pm 0.036$ mag and $(H - K_s)_2 = 0.039 \pm 0.029$ mag. The infrared colors of the primary star are consistent with an early-G or late-F main-sequence star, in agreement with the derived stellar parameters. The companion star has infrared colors that are consistent with a later G-type main-sequence star.

Based on the *TESS* magnitude and 2MASS color relationships established for the *TESS* Input Catalog (Stassun et al. 2018), we

**Figure 2.** AO image (inset) and *K_s*-band contrast curves for HD 202772A, obtained with Keck/NIRC2. A companion is visible 1^h/3 northwest of the primary. The black line is the 5 σ sensitivity, with a 1 σ scatter marked in purple. See the text for further details.

estimate the deblended *TESS* magnitudes for the two components to be $T_1 = 7.92 \pm 0.09$ mag and $T_2 = 9.62 \pm 0.09$ mag for a *TESS* magnitude difference of $\Delta_T = 1.70 \pm 0.13$ mag and a *TESS* flux ratio of $F_2/F_1 = 0.21 \pm 0.02$. We used this value of the flux ratio to correct the apparent transit depth in the *TESS* light curve and derive the unblended transit depth.

We will refer to the brighter target (hosting the planet) as HD 202772A and the fainter companion as HD 202772B. Given the similarity between the two stars, and a projected separation of only ~ 200 au, it seems very likely that the two stars are gravitationally bound. The chance alignment probability is negligible, as estimated from the Besanon Galactic Model (Robin et al. 2003). We have also checked all 131 stars in the *Gaia* DR2 catalog within 300 $''$ of HD 202772A with

Table 2
HD 202772A

Parameter	SMARTS 1.5 m/CHIRON	FLWO 1.5 m/TRES	LCO/NRES	KECK/HIRES	EXOFASTv2 FIT
T_{eff} [K]	6470 ± 100	6270 ± 50	6255 ± 100	6330 ± 100	6272_{-71}^{+77}
$\log g_*$ [cgs]	3.90 ± 0.15	3.91 ± 0.10	4.0 ± 0.1	4.03 ± 0.10	$3.848_{-0.027}^{+0.030}$
[Fe/H] [dex]	0.30 ± 0.10	0.16 ± 0.08	0.27 ± 0.06	0.29 ± 0.06	0.300 ± 0.060
M_* [M_{\odot}]	1.73 ± 0.05	...	$1.78_{-0.06}^{+0.02}$	$1.69_{-0.04}^{+0.05}$	$1.720_{-0.066}^{+0.064}$
R_* [R_{\odot}]	2.65 ± 0.15	...	$2.87_{-0.10}^{+0.11}$	$2.515_{-0.127}^{+0.137}$	$2.594_{-0.090}^{+0.076}$
Age [Gyr]	1.6 ± 0.1	...	$1.48_{-0.16}^{+0.24}$	$1.52_{-0.20}^{+0.19}$	$1.70_{-0.26}^{+0.32}$
$V \sin i$ [km s^{-1}]	...	8.1 ± 0.5	5.5 ± 1.4	7.0 ± 1.0	...

Note.¹The spectroscopic priors on T_{eff} and [Fe/H] from Keck/HIRES are imposed in the EXOFASTv2 analysis.

measured parallax and proper motion, and the only nearby source with a similar projected velocity is HD 202772B.

2.3. Las Cumbres Observatory (LCO)/Network of Echelle Spectrographs (NRES) Optical Spectroscopy

To obtain independent estimates of the stellar parameters, we performed high-resolution optical spectroscopy with the LCO robotic network of telescopes (Brown et al. 2013). We obtained three 20-minute exposures with a total signal-to-noise ratio (S/N) ≈ 100 with the NRES (Sivard et al. 2016, 2018) mounted on a 1.0 m telescope at the South African Astronomical Observatory.

Since the NRES fiber diameter corresponds to $2''8$, it captured the light from both stars in the visual binary system. Using TODCOR (Zucker & Mazeh 1994), we identified two RV components separated by $5.8 \pm 1.0 \text{ km s}^{-1}$. This RV difference is compatible with the order of magnitude of the RV variation one would expect from the orbital motion of the stars, given their masses and sky-projected separation. The stellar parameters derived from collected spectra are listed in Table 2.

2.4. Keck/HIRES Optical Spectroscopy

In order to obtain a spectrum of each of the two stars with minimal contamination from the other star, we observed both stars with Keck/HIRES (Vogt et al. 1994) on 2018 September 23. We obtained one spectrum of each star, with the HIRES slit oriented perpendicular to the separation between the two stars. Given the angular separation between the two stars, the slit width ($0''86$), and the astronomical seeing at Keck at the night of the observation ($\approx 0''7$), the level of cross-contamination is expected to be less than 10%. Both spectra were obtained without the iodine (I_2) cell, at a spectroscopic resolution of $R \approx 65000$, and at an S/N per pixel of 150 at 5500 \AA . A similar technique was successfully applied by Shporer et al. (2014) to a visual binary system in which both members have similar brightness and a smaller angular separation.

2.5. Doppler Velocimetry with CHIRON

We obtained a total of 14 spectra of HD 202772A using CHIRON (Tokovinin et al. 2013), a fiber-fed high-resolution optical spectrograph mounted on the SMARTS 1.5 m telescope at Cerro Tololo in Chile. We collected the spectra using the image slicer, which delivers a resolution of ~ 80000 and a higher throughput than the standard slit mode. Our 15 minutes exposures yielded an S/N per pixel of ~ 60 – 80 at 5500 \AA .

Although CHIRON is equipped with an iodine cell to obtain a precise wavelength solution that permits long-term RV

precision better than ~ 2 – 3 m s^{-1} (e.g., Jones et al. 2017), we did not use the iodine cell for these observations. This is because the cell absorbs $\sim 25\%$ of the light at 5500 \AA , significantly decreasing the S/N. Moreover, using the I_2 cell requires a time-consuming acquisition of a high-S/N template spectrum of the target star.

Instead, we derived the RVs using the Cross-Correlation-Function (CCF) method, in a manner similar to Jones et al. (2017). CHIRON is not equipped with a simultaneous calibration fiber. Instead, we acquired a Th-Ar lamp exposure before and after each target exposure. We computed the wavelength solution for the target spectra by interpolating line positions for the lamps to match the temporal midpoint of each observation. We thereby achieved an RV stability of ~ 5 – 6 m s^{-1} , which was verified with two RV standard stars observed nightly. The resulting RVs of HD 202772A are listed in Table 3. RVs collected by CHIRON show a $\sim 95 \text{ m s}^{-1}$ sinusoidal variation in phase with the transit ephemeris.

Finally, from the CCF, we measured the bisector velocity span (BVS) and FWHM variations, to check on the possibility that the observed RV variation results from stellar activity or a background eclipsing binary system (see, e.g., Santerne et al. 2015).

The CHIRON fiber has a $2''7$ diameter on the sky, but HD 202772A and B are separated by only $1''3$, which means that we must expect some of the light from the binary companion to be present in the spectra. Given that the two stars have a similar radial velocity, there is a risk that the stationary CCF of the binary companion causes the apparent amplitude of the RV variation to be lower than the true RV variation of the planet host. Such a “peak pulling” effect was observed in a study of the Kepler-14 system (Buchhave et al. 2011). We note, however, that HD 202772B is fainter than HD 202772A and only emits about 20% of the total light from the binary system. As described in Section 2.7, we did not find any evidence that the RVs from CHIRON were significantly affected by light contamination from HD 202772B.

2.6. Doppler Velocimetry with FLWO 1.5 m/Tillinghast Reflector Echelle Spectrograph (TRES)

We obtained 12 spectra of HD 202772A with the TRES (Fűrész et al. 2008) on the 1.5 m Tillinghast Reflector at Fred L. Whipple Observatory (FLWO) on Mt. Hopkins, AZ between UT 2018 September 14 and UT 2018 September 30. TRES is a fiber-fed, cross-dispersed echelle spectrograph with a resolving power of $R \sim 44000$ and an instrumental precision of ~ 10 – 15 m s^{-1} . The typical exposure time was ~ 4 minutes, resulting in S/N per resolution element of ~ 75 at 5200 \AA . The

Table 3
Relative Radial Velocities for HD 202772A

BJD -2458300	RV (m s ⁻¹)	σ_{RV} (m s ⁻¹)	BVS ¹ (m s ⁻¹)	σ_{BVS} (m s ⁻¹)	FWHM ^a (m s ⁻¹)	σ_{FWHM} (m s ⁻¹)	Instrument
69.5363	-87.5	7.5	15.4	20.1	16302.0	141.5	CHIRON
69.7550	-52.0	6.2	15.4	11.3	16258.7	128.1	CHIRON
70.5656	68.7	4.9	32.6	23.2	16279.1	130.0	CHIRON
71.5411	29.5	8.9	17.1	19.0	16133.5	132.2	CHIRON
71.6964	11.2	6.3	39.4	16.5	16171.8	130.5	CHIRON
72.5988	-76.2	5.4	25.7	18.1	16274.6	132.2	CHIRON
73.6179	50.1	5.5	22.3	15.0	16225.0	133.9	CHIRON
79.6314	-49.4	4.8	-15.4	15.5	16292.1	131.5	CHIRON
79.7038	-54.5	5.7	34.3	20.5	16320.8	133.3	CHIRON
79.7466	-49.3	9.8	15.4	19.0	16243.6	132.4	CHIRON
80.5925	80.0	6.7	-8.6	21.7	16264.7	140.5	CHIRON
80.6924	72.3	11.1	-30.9	25.3	16162.8	154.1	CHIRON
81.5400	-24.9	13.6	20.6	35.9	16166.2	136.7	CHIRON
83.6838	81.7	7.7	60.0	17.5	16229.4	127.2	CHIRON
83.5215	34.8	2.0	HARPS
83.5252	36.3	2.0	HARPS
84.5863	80.3	2.0	HARPS
84.5837	97.8	2.4	HARPS
85.5194	-90.3	2.8	HARPS
85.5128	-96.0	2.8	HARPS
85.7274	-62.7	2.0	HARPS
75.7239	-0.5	12.0	-4.6	12.8	18858	151	TRES
77.6977	174.7	19.8	-10.4	19.4	18997	231	TRES
79.7226	56.6	14.9	-25.4	8.3	18861	149	TRES
82.7170	0.0	12.0	-11.4	8.3	18869	144	TRES
83.7441	231.0	16.1	5.7	19.6	18673	222	TRES
84.7374	154.6	20.2	-20.6	23.7	18843	137	TRES
86.7178	124.7	17.0	5.5	11.6	18831	112	TRES
87.6938	163.5	21.3	38.3	14.7	18944	157	TRES
88.6862	20.2	17.4	22.0	24.4	18909	218	TRES
89.7004	72.1	16.2	-9.3	12.6	18796	109	TRES
90.7214	203.7	18.7	-4.1	8.3	18814	153	TRES
91.6617	30.3	20.1	14.4	11.7	18966	132	TRES

Note.

^a The HARPS BVS and FWHM are not listed because those measurements were corrupted by moonlight (Section 2.7).

spectra are calibrated using a Th-Ar lamp, exposed through the science fiber before and after each set of science exposures. We note that the TRES fiber is 2''3, and the exposures therefore include light from HD 202772B.

We reduced and analyzed the spectra according to the procedures outlined in Buchhave et al. (2010). Namely, the spectra were optimally extracted and then cross-correlated, order by order, against the strongest spectrum of HD 202772A. We exclude spectral orders far to the blue where the S/N is low, in the red where telluric lines contaminate the spectrum, and a few orders in between with little information content or affected by broad feature (e.g., Balmer lines) toward the edge of the order that affect continuum fitting. RVs were ultimately derived from a region spanning 4130–6280 Å. The peak of the summed CCF across all orders is fit to derive the final RV, and the scatter between orders within each spectrum is taken to be the internal error estimate. These relative RVs and their uncertainties are reported in Table 3.

We also derive the BVS and FWHM from the cross-correlation function of each spectrum against a non-rotating synthetic spectrum with appropriate T_{eff} , $\log g_*$, and [Fe/H].

These values are also reported in Table 3 and shown in Figure 6, and show no correlation with the RVs.

2.7. Doppler Velocimetry with High Accuracy Radial velocity Planet Searcher (HARPS)

To provide further confirmation of the planetary origin of the transit signal, we obtained nine spectra using the HARPS (Mayor et al. 2003).

These data were obtained simultaneously with Th-Ar reference spectra during three consecutive nights in good seeing conditions ($\lesssim 1''.0$). Exposure time was 200–300 seconds, leading to an S/N of ~ 70 –80 at 6000 Å. We carefully centered the brighter star within the 1'' aperture fiber, to ensure that no light contamination from the companion was reaching the detector. We also carefully adjusted the size of the guiding box, to avoid guiding problems due to the secondary star, which was clearly visible in the acquisition camera. During the HARPS observations, the Moon was between 13° and 36° from our target, with an illuminated fraction between 92% and 99%. This led to some lunar contamination in the spectra. Moreover, the RV of the Moon was very close to the RV of the target star,

which severely affected the shape of the CCF. For this reason, we discarded the two RV data points that were most affected and had very deviant values. Also, due to the contamination, the derived BVS and FWHM of the CCF are not reliable, and are not listed in Table 3. We processed the HARPS data using the CERES code (Brahm et al. 2017). The derived RVs from the CERES code also agree well with those from the SERVALL pipeline (Zechmeister et al. 2018). The resulting RVs are listed in Table 3 and also shown in Figure 4. As can be seen, the HARPS data agree with the CHIRON data, although the scatter around the fit is larger than expected. This is most likely caused by the lunar light contamination.

3. Stellar Parameters

3.1. Results from CHIRON

To derive the stellar atmospheric parameters of HD 202772A, we measured the equivalent widths (EWs) of about 150 relatively weak Fe I and Fe II absorption lines ($EW \lesssim 120 \text{ m\AA}$). The EWs were measured in the high-S/N template obtained by stacking the individual spectra (see Section 2.5), using the ARES v2 automatic tool (Sousa et al. 2015).

We then used the MOOG code (Snedden 1973) along with the Kurucz (1993) stellar atmosphere models to solve the radiative transfer equations under the assumptions of local excitation and ionization equilibrium via the Saha and Boltzmann equations. For each iron line, MOOG computes the corresponding iron abundance by matching the measured EW in the curve of growth computed from the input stellar model. This procedure is performed iteratively for models with different effective temperatures (T_{eff}), iron abundances ($[\text{Fe}/\text{H}]$), and microturbulent velocities (V_{micro}) until there is no correlation between the line excitation potential and wavelength with the model abundance. Finally, we obtained the surface gravity ($\log g_*$) using the constraint that the iron abundances derived from both the Fe I and Fe II lines should be the same (for a more thorough description of the procedure, see Jones et al. 2011). Table 2 gives the resulting stellar parameters.

We computed the luminosity of HD 202772A based on the *Gaia* DR2 parallax ($\pi = 6.166 \pm 0.092$, *Gaia* Collaboration et al. 2018), the apparent V magnitude (after correcting for interstellar absorption by $A_V = 0.10 \text{ mag}$), and the bolometric correction of Alonso et al. (1999). Using this information and the stellar atmospheric parameters (T_{eff} and $[\text{Fe}/\text{H}]$), we derived the stellar physical parameters using the PARSEC stellar-evolutionary models (Bressan et al. 2012). The results are also listed in Table 2.

3.2. Results from FLWO 1.5 m/TRES

We used the Spectral Parameter Classification (SPC) tool (Buchhave et al. 2012) to derive stellar parameters from the TRES spectra. We allowed T_{eff} , $\log g_*$, $[\text{Fe}/\text{H}]$, and $V \sin i$ to be free parameters. SPC works by cross correlating an observed spectrum against a grid of synthetic spectra based on Kurucz atmospheric models (Kurucz 1993). The weighted average results are listed in Table 2.

3.3. Results from LCO/NRES

We analyzed the LCO/NRES spectrum using the methodology of Fulton & Petigura (2018). We measured T_{eff} , $\log g_*$,

$[\text{Fe}/\text{H}]$, and $V \sin i$ using SpecMatch (Petigura 2015),³⁸ which compares the observed spectrum with a grid of model spectra (Coelho et al. 2005). The resulting parameters are listed in Table 2.

To calculate the star’s physical parameters, we used *isoclassify* (Huber et al. 2017), which takes as input the effective temperature, metallicity, parallax, and apparent K_s magnitude. Using the *isoclassify* “direct” mode, we calculated the posterior probability distributions for R_* and L_* by applying the Stefan-Boltzmann law. Using the *isoclassify* “grid” mode, we calculated the range of MIST isochrone models (Choi et al. 2016; Dotter 2016) that are consistent with the spectroscopic parameters to estimate the stellar mass and age. The results of the SpecMatch+*isoclassify* analysis are listed in Table 2.

3.4. Results from Keck/HIRES

To compute stellar parameters from Keck/HIRES spectrum for each of the two stars, we used the same technique (SpecMatch+*isoclassify*) that was applied on NRES spectra.

The resulting atmospheric and physical stellar parameters obtained from SpecMatch+*isoclassify* analysis for both HD 202772A and B are listed in Tables 1 and 2.

The stellar parameters derived from resolved HIRES spectra show good agreement with those from the CHIRON, TRES, and NRES spectra, except that TRES finds modestly lower $[\text{Fe}/\text{H}]$. Evidently, the contaminating light from the secondary star in the CHIRON, TRES, and NRES spectra did not strongly affect the determination of the basic stellar parameters.

4. Planetary System Parameters from Global Analysis

We performed a joint analysis of the *TESS* data, the RV data, the spectroscopic priors on T_{eff} and $[\text{Fe}/\text{H}]$ from Keck, and the stellar spectral energy distribution using EXOFASTv2³⁹ (Eastman et al. 2013; Eastman 2017).

The stellar limb-darkening function was assumed to be quadratic, with the coefficients fit with a prior from Claret (2018) for the *TESS* band based on the T_{eff} , $\log g_*$, and $[\text{Fe}/\text{H}]$ at each step, with a Gaussian uncertainty of 0.05 for each parameter. As is evident in Table 4, the resulting uncertainties are smaller than this, indicating the transit itself was a stronger constraint on the limb-darkening parameters.

We imposed Gaussian priors on the *Gaia* DR2 parallax of $6.77 \pm 0.11 \text{ mas}$ (after adjusting by $82 \mu\text{as}$ as advocated by Stassun et al. 2018) and the *TESS*-band dilution from the neighboring star of 0.21 ± 0.02 found from the AO imaging. We imposed an upper limit on the V -band extinction of 0.17236 from Schlafly & Finkbeiner (2011). The priors for all the remaining parameters were uniform and unbounded.

The stellar parameters are simultaneously constrained by the transit light curve, the SED, the MIST isochrones, and the Keck spectroscopic priors on T_{eff} and $[\text{Fe}/\text{H}]$. The global model fits an R_* , M_* , T_{eff} , $\log g_*$, $[\text{Fe}/\text{H}]$, distance, and age, which self consistently informs all three models, and the MCMC optimizes each parameter. The light curve is a constraint on the stellar density, the SED primarily constrains the stellar radius and T_{eff} , and a penalty for straying from the MIST stellar

³⁸ <https://github.com/petigura/specmatch-syn>

³⁹ <https://github.com/jdeast/EXOFASTv2>

Table 4
Median Values and 68% Confidence Interval for HD 202772A Planetary System

Parameter	Units	Values		
Stellar Parameters:				
M_* ...	Mass (M_\odot)...	$1.720^{+0.064}_{-0.066}$		
R_* ...	Radius (R_\odot)...	$2.591^{+0.078}_{-0.093}$		
L_* ...	Luminosity (L_\odot)...	$9.36^{+0.54}_{-0.58}$		
ρ_* ...	Density (cgs)...	$0.140^{+0.015}_{-0.012}$		
$\log g$...	Surface gravity (cgs)...	$3.848^{+0.030}_{-0.027}$		
T_{eff} ...	Effective Temperature (K)...	6272^{+77}_{-71}		
[Fe/H]...	Metallicity (dex)...	0.300 ± 0.060		
Age...	Age (Gyr)...	$1.70^{+0.32}_{-0.26}$		
A_V ...				
ϖ_{SED} ...				
ϖ ...	Parallax (mas)...	6.80 ± 0.11		
d ...	Distance (pc)...	$147.2^{+2.5}_{-2.4}$		
Planetary Parameters:				
P ...	Period (days)...	3.308958 ± 0.000083		
R_p ...	Radius (R_J)...	$1.545^{+0.052}_{-0.060}$		
T_C ...	Time of conjunction (BJD _{TDB})...	$2458328.68359^{+0.00035}_{-0.00036}$		
T_0 ...	Optimal conjunction Time (BJD _{TDB})...	$2458338.61047 \pm 0.00024$		
a ...	Semimajor axis (au)...	$0.05208^{+0.00064}_{-0.00068}$		
i ...	Inclination (Degrees)...	$84.51^{+1.1}_{-0.82}$		
e ...	Eccentricity ...	$0.038^{+0.042}_{-0.027}$		
ω_* ...	Argument of Periastron (Degrees)...	98^{+65}_{-52}		
T_{eq} ...	Equilibrium temperature (K)...	2132^{+28}_{-30}		
M_p ...	Mass (M_J)...	$1.017^{+0.070}_{-0.068}$		
K ...	RV semi-amplitude (m s^{-1})...	$96.4^{+6.2}_{-6.0}$		
R_p/R_* ...	Radius of planet in stellar radii ...	$0.06128^{+0.00083}_{-0.00081}$		
a/R_* ...	Semimajor axis in stellar radii ...	$4.33^{+0.15}_{-0.13}$		
δ ...	Transit depth (fraction)...	$0.003755^{+0.00010}_{-0.000099}$		
τ ...	Ingress/egress transit duration (days)...	0.0162 ± 0.0011		
T_{14} ...	Total transit duration (days)...	$0.2346^{+0.0011}_{-0.0011}$		
b ...	Transit Impact parameter ...	$0.403^{+0.058}_{-0.084}$		
ρ_p ...	Density (cgs)...	$0.343^{+0.043}_{-0.035}$		
$\log g_p$...	Surface gravity ...	$3.025^{+0.038}_{-0.036}$		
$\langle F \rangle$...	Incident Flux ($10^9 \text{ erg s}^{-1} \text{ cm}^{-2}$)...	$4.68^{+0.25}_{-0.26}$		
T_p ...	Time of Periastron (BJD _{TDB})...	$2458328.75^{+0.56}_{-0.45}$		
T_S ...	Time of eclipse (BJD _{TDB})...	$2458330.332^{+0.040}_{-0.051}$		
$\cos\omega_*$	$-0.003^{+0.019}_{-0.024}$		
$e \sin\omega_*$	$0.025^{+0.048}_{-0.026}$		
$M_p \sin i$...	Minimum mass (M_J)...	$1.013^{+0.070}_{-0.068}$		
M_p/M_* ...	Mass ratio ...	$0.000565^{+0.000037}_{-0.000035}$		
d/R_* ...	Separation at mid transit ...	$4.21^{+0.25}_{-0.30}$		
Wavelength Parameters:				
u_1 ...	linear limb-darkening coeff ...	$0.216^{+0.030}_{-0.031}$		
u_2 ...	quadratic limb-darkening coeff ...	$0.279^{+0.044}_{-0.043}$		
A_D ...	Dilution from neighboring stars ...	0.209 ± 0.020		
Telescope Parameters:				
γ_{rel} ...	Relative RV Offset (m s^{-1})...	Chiron $-17892.8^{+4.6}_{-5.1}$	HARPS 9 ± 11	TRES $98.4^{+8.7}_{-8.9}$
σ_J ...	RV Jitter (m s^{-1})...	$14.7^{+5.6}_{-4.1}$	$26.8^{+15}_{-8.5}$	$24.5^{+11}_{-8.4}$

Note.¹ Assuming zero albedo and full heat distribution from day to night hemispheres.

tracks ensure the resulting star is physical. The resulting stellar parameters are listed in Table 2 and show good agreement with the results of the spectroscopic analysis.

The best-fitting model is plotted in Figures 3–5 and listed in Table 4. In particular, we find the star to be $1.7 M_\odot$, $2.6 R_\odot$, and the planet to be $1.6 R_J$, $1.0 M_J$ with a relatively low mean density of 0.34 g cm^{-3} . The fitted eccentricity is consistent

with zero, which is expected for a planet with a period of 3.3 days. Further RV follow-up would be very useful in understanding the small structure in the residual. With an independent analysis, we did not detect any Transit Timing Variations at a level above 52 s, so in the final global fit, we assumed a linear ephemeris. Figure 6 shows the BVS and FWHM as a function of the measured radial velocities. There is

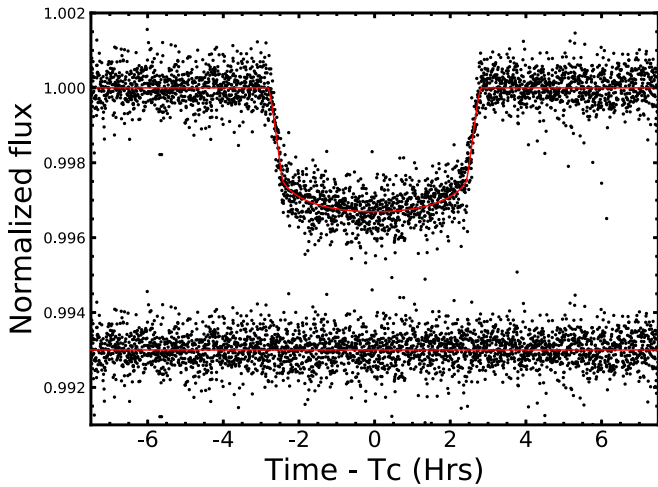


Figure 3. Phased light curves of HD 202772A b. The red solid line represents the best-fitting model. The residuals from the best fit are plotted below.

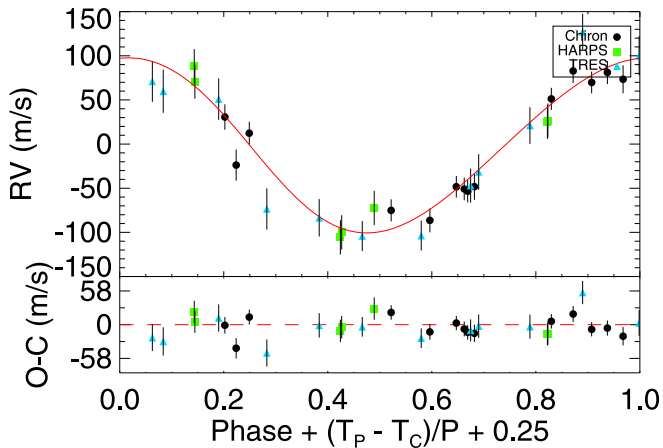


Figure 4. RV measurements from CHIRON (black circles), HARPS (green squares), and TRES (blue triangles) as a function of orbital phase. The error bars include the fitted jitter term. The units of the horizontal axis are chosen so the time of transit is at 0.25. The solid red line is the best-fitting model, based on the transit photometry as well as the RV data. The fitted value of the systemic velocity has been subtracted from both the RVs and the model. The bottom panel presents the residuals between the data and the best-fit model.

no significant correlation between these quantities and the radial velocities.

5. Discussion

HD 202772A b is an inflated Jupiter-mass planet orbiting a metal-rich star with an orbital period of 3.3 days. The red dots in Figure 7 show the location of this newly discovered planet in the spaces of planetary mass, radius, and incident flux, compared with the current sample of transiting giant planets. HD 202772A b is one of the largest known planets, with a relatively low mean density of 0.34 g cm^{-3} . It is also one of the most strongly irradiated planets, thereby obeying the well-known correlation between planetary radius and degree of irradiation (see, e.g., Laughlin et al. 2011; Lopez & Fortney 2016). Based on the irradiation of $4.68 \times 10^9 \text{ erg s}^{-1} \text{ cm}^{-2}$, the estimated equilibrium temperature is about 2100 K (see Table 4).

The large size of HD 202772A b might be connected to the evolutionary state of the host star (Grunblatt et al. 2017). Figure 8 shows the location of HD 202772A in the space of

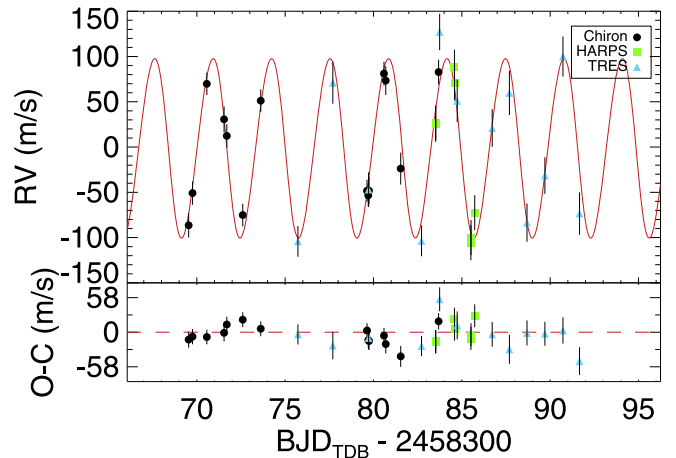


Figure 5. Same as Figure 4 but as a function of time instead of orbital phase.

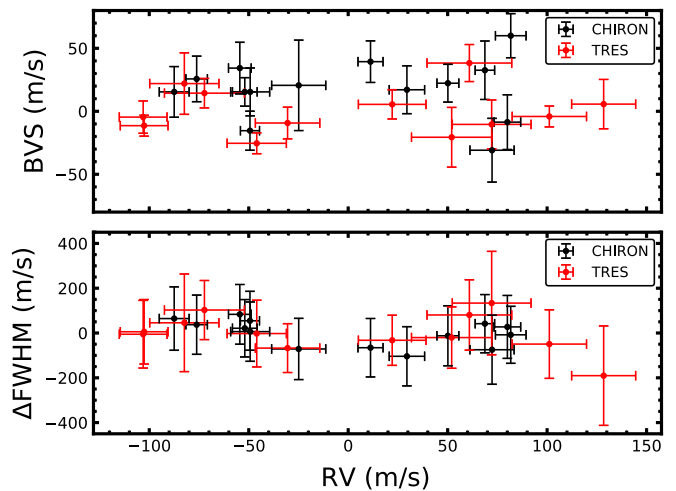


Figure 6. Bisector velocity span (BVS; top panel) and CCF FWHM (bottom panel) as functions of the radial velocities collected by SMARTS 1.5 m/CHIRON and FLWO 1.5 m/TRES.

surface gravity and effective temperature. HD 202772A is slightly evolved, with a relatively low surface gravity. As a star evolves, its luminosity increases, which also increases the flux of radiation impinging on any planets. If giant planets are “inflated” by intense stellar radiation, as has long been proposed, then the larger-than-usual size of HD 202772A b suggests that the evolutionary timescale of the star is slower than the inflationary timescale of the planet.

Thanks to the extended atmosphere of the planet, its bright host star, and its long transit duration, a single transit observation of HD 202772A b is expected to yield signal-to-noise levels for atmospheric spectral features that are in the top 10 of all known transiting planets (based on the transmission metric from Kempton et al. 2018, and planets retrieved from the NASA Exoplanet Archive).

Because of its relatively high equilibrium temperature ($T_{\text{eq}} = \sim 2100 \text{ K}$) and its relatively short orbital period, HD 202772A b also provides one of the best opportunities (Niraula et al. 2017), behind only WASP-33 (Gaudi et al. 2017) and WASP-12 (Stevenson et al. 2014; Jensen et al. 2018), of probing the atmospheric properties of a very hot gas giant ($R_p > 4R_{\oplus}$, $T_{\text{eq}} > 2100 \text{ K}$).

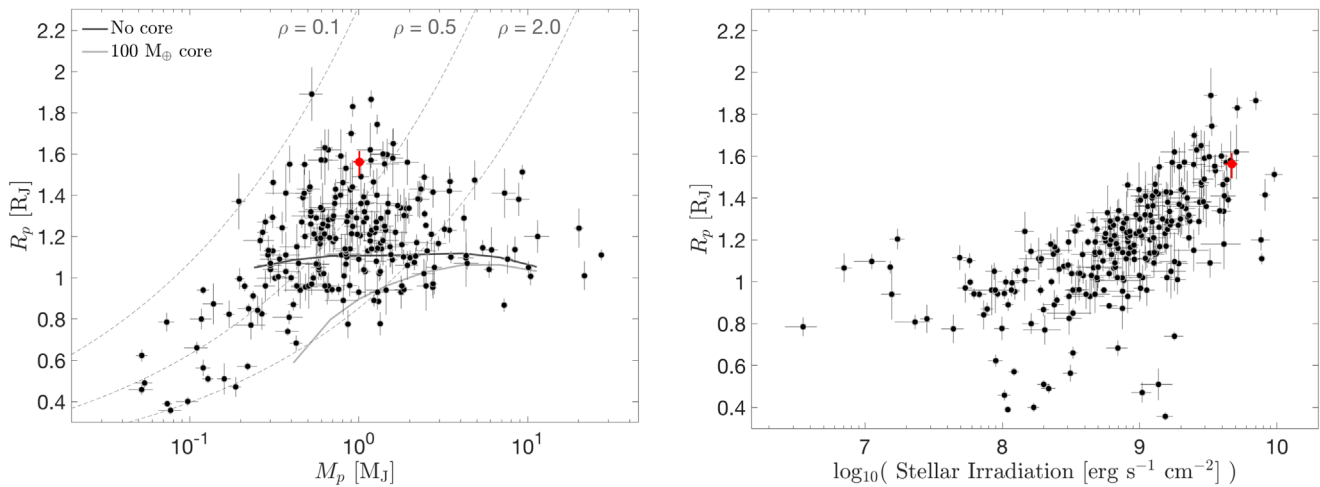


Figure 7. The position of HD 202772A b (red) in the space of mass, radius, and irradiation, compared to the population of known transiting gas giant planets (black). In the left panel, the solid lines mark theoretical models taken from Baraffe et al. (2014) for no core (black) and a $100 M_{\text{Earth}}$ core (gray). The dashed lines are isodensity contours. Data were obtained from the NASA Exoplanet Archive (Akeson et al. 2013) on 2018 September 15.

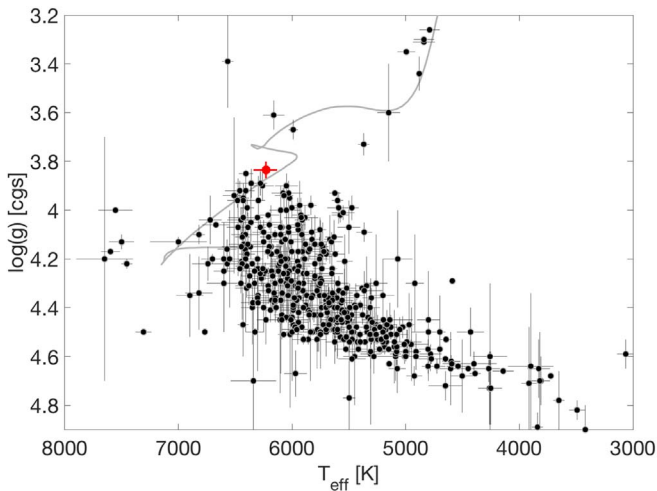


Figure 8. Surface gravity and effective temperature of the hosts of transiting giant planets (similar to an H–R diagram). The position of HD 202772A (red) falls near the edge of the occupied region of parameter space. The solid gray line is the best-fitting MIST stellar mass track of $1.721 M_{\odot}$. We estimate that the stellar age is 1.71 Gyr, and that it is going to leave its main-sequence life in ~ 0.5 Gyr. Data were obtained from the NASA Exoplanet Archive (Akeson et al. 2013) on 2018 September 15.

The planet’s hot atmosphere lends to its suitability for thermal emission measurements; secondary eclipse observations for this system are already being planned as part of *Spitzer* Program 14084 (PI: I. Crossfield). The combination of transmission and emission spectroscopy has the potential to yield precise constraints on exoplanetary climates and atmospheric compositions; however, few known systems are good targets for both types of measurements (Kreidberg et al. 2014). The discovery of HD 202772A b is therefore an important addition to the roster of transiting planets, with the strong potential to shed light on the atmospheric physics and chemistry of gas giants.

HD 202772A will exhaust its hydrogen fuel in ~ 0.5 Gyr, which may have ramifications for the survival of the planet. The apparent paucity of hot Jupiters orbiting evolved stars (Johnson et al. 2007) has been interpreted as a consequence of

tidal destruction (Villaver & Livio 2009; Schlaufman & Winn 2013). Tides raised on the star by the planet cause the planet to transfer angular momentum to the star, a process that is thought to accelerate rapidly as the star grows in size. However, the timescale for this process is unknown, with an uncertainty spanning several orders of magnitude.

The recent discoveries of close-in gas giants around subgiants (e.g., Van Eylen et al. 2016), or even red giants (e.g., Jones et al. 2018) suggest that the lifetimes of hot Jupiters in those systems may not be as short as previously thought. Alternatively, as predicted by Stephan et al. (2018), the eccentric Kozai–Lidov mechanism in a binary stellar system can drive a longer-period Jupiter to migrate inward during the post-main-sequence phase. It seems that with the distant stellar companion, HD 202772A b is consistent with this scenario. A likely prediction from this scenario is that HD 202772A b may have a non-zero stellar obliquity (the angle between the orbital axis and the stellar spin axis), which can be tested in future observations. From the stellar and planetary parameters we obtained, we predict that the Rossiter-McLaughlin effect will have an RV semi-amplitude of 10.5 m s^{-1} (e.g., Winn et al. 2005; Gaudi & Winn 2007; Albrecht et al. 2012; Wang et al. 2018).



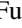





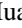



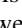

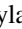

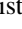
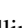
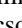
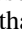

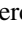

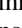


However, it is impossible to draw any firm conclusions until we can measure the occurrence rates of such planets using a homogeneous data set. The *TESS* survey should eventually provide the opportunity to perform such a study, by detecting thousands of new planets orbiting a wider variety of stars than were observed in the *Kepler* mission.

We thank the anonymous referee for the insightful suggestions that greatly improved this manuscript. We thank Yanqin Wu, Smadar Naoz, Ian Crossfield, Lars A. Buchhave, Bonan Pu, Alexander P. Stephan, Sabarni Basu, Xi Zhang, Beibei Liu, and Jorge Lillo-Box for their insights. J.N.W. and S.W. thank the Heising-Simons Foundation for their generous support. M.N.G. acknowledges support from MIT’s Kavli Institute as a Torres postdoctoral fellow. S.M. and A.B.D. are supported by the National Science Foundation Graduate Research Fellowship Program under Grant Number DGE-1122492. R.B. acknowledges support from FONDECYT

Postdoctoral Fellowship Project 3180246, and from the Millennium Institute of Astrophysics (MAS). G.L. acknowledges support from the National Aeronautics and Space Administration through the NASA Astrobiology Institute under Cooperative Agreement Notice NNH13ZDA017C issued through the Science Mission Directorate. This research is based on observations collected at the European Organization for Astronomical Research in the Southern Hemisphere under ESO programme 0101.C-0232. This work makes use of observations from SMARTS and the LCO network. We acknowledge the use of public *TESS* Alert data from pipelines at the *TESS* Science Office and at the *TESS* Science Processing Operations Center. Funding for the *TESS* mission is provided by NASA's Science Mission directorate. The authors wish to recognize and acknowledge the very significant cultural role and reverence that the summit of Maunakea has always had within the indigenous Hawaiian community. We are most fortunate to have the opportunity to conduct observations from this mountain. This research has made use of the Exoplanet Follow-up Observation Program website and the NASA Exoplanet Archive, which is operated by the California Institute of Technology, under contract with the National Aeronautics and Space Administration under the Exoplanet Exploration Program. This paper includes data collected by the *TESS* mission, which are publicly available from the Mikulski Archive for Space Telescopes (MAST). We made use of the Python programming language (Rossum 1995) and the open-source Python packages NUMPY (van der Walt et al. 2011), EMCEE (Foreman-Mackey et al. 2013), and CELERITE (Foreman-Mackey et al. 2017).

Facilities: *TESS*, CTIO:1.5 m (CHIRON), ESO:3.6 m (HARPS), Keck II (NIRC2), Keck I (HIRES), LCO:1.0 m (NRES), FLWO:1.5 m (TRES).

ORCID iDs

Songhu Wang  <https://orcid.org/0000-0002-7846-6981>
 Avi Shporer  <https://orcid.org/0000-0002-1836-3120>
 Benjamin J. Fulton  <https://orcid.org/0000-0003-3504-5316>
 Trifon Trifonov  <https://orcid.org/0000-0002-0236-775X>
 Jason Eastman  <https://orcid.org/0000-0003-3773-5142>
 Seth Redfield  <https://orcid.org/0000-0003-3786-3486>
 Maximilian N. Günther  <https://orcid.org/0000-0002-3164-9086>
 Laura Kreidberg  <https://orcid.org/0000-0003-0514-1147>
 Chelsea X. Huang  <https://orcid.org/0000-0003-0918-7484>
 Sarah Millholland  <https://orcid.org/0000-0003-3130-2282>
 Debra Fischer  <https://orcid.org/0000-0003-2221-0861>
 Rafael Brahm  <https://orcid.org/0000-0002-9158-7315>
 Allen B. Davis  <https://orcid.org/0000-0002-5070-8395>
 John M. Brewer  <https://orcid.org/0000-0002-9873-1471>
 Hui Zhang  <https://orcid.org/0000-0003-3491-6394>
 Allyson Bieryla  <https://orcid.org/0000-0001-6637-5401>
 Timothy M. Brown  <https://orcid.org/0000-0001-5062-0847>
 Jessie L. Christiansen  <https://orcid.org/0000-0002-8035-4778>
 Karen A. Collins  <https://orcid.org/0000-0001-6588-9574>
 Howard Isaacson  <https://orcid.org/0000-0002-0531-1073>
 David W. Latham  <https://orcid.org/0000-0001-9911-7388>
 Samuel N. Quinn  <https://orcid.org/0000-0002-8964-8377>
 Robert J. Siverd  <https://orcid.org/0000-0001-5016-3359>
 Roland Vanderspek  <https://orcid.org/0000-0001-6763-6562>
 Joshua N. Winn  <https://orcid.org/0000-0002-4265-047X>
 Jon M. Jenkins  <https://orcid.org/0000-0002-4715-9460>

Patricia T. Boyd  <https://orcid.org/0000-0003-0442-4284>
 Martin Paegert  <https://orcid.org/0000-0001-8120-7457>
 Keivan G. Stassun  <https://orcid.org/0000-0002-3481-9052>
 Gregory Laughlin  <https://orcid.org/0000-0002-3253-2621>

References

- Akeson, R. L., Chen, X., Ciardi, D., et al. 2013, *PASP*, 125, 989
 Albrecht, S., Winn, J. N., Johnson, J. A., et al. 2012, *ApJ*, 757, 18
 Alonso, A., Arribas, S., & Martínez-Roger, C. 1999, *A&A*, 140, 261
 Baraffe, I., Chabrier, G., Fortney, J., & Sotin, C. 2014, in *Protostars and Planets VI*, ed. H. Beuther et al. (Tucson, AZ: Univ. Arizona Press), 763
 Barclay, T., Pepper, J., & Quintana, E. V. 2018, *ApJS*, 239, 2
 Batygin, K., Bodenheimer, P. H., & Laughlin, G. P. 2016, *ApJ*, 829, 114
 Becker, J. C., Vanderburg, A., Adams, F. C., Rappaport, S. A., & Schwengeler, H. M. 2015, *ApJL*, 812, L18
 Bodenheimer, P., Hubickyj, O., & Lissauer, J. J. 2000, *Icar*, 143, 2
 Bonomo, A. S., Desidera, S., Benatti, S., et al. 2017, *A&A*, 602, A107
 Brahm, R., Jordán, A., & Espinoza, N. 2017, *PASP*, 129, 034002
 Bressan, A., Marigo, P., Girardi, L., et al. 2012, *MNRAS*, 427, 127
 Gaia Collaboration, Brown, A. G. A., Vallenari, A., et al. 2018, *A&A*, 616, A1
 Brown, T. M., Baliber, N., Bianco, F. B., et al. 2013, *PASP*, 125, 1031
 Buchhave, L. A., Bakos, G. Á, Hartman, J. D., et al. 2010, *ApJ*, 720, 118
 Buchhave, L. A., Latham, D. W., Carter, J. A., et al. 2011, *ApJS*, 197, 3
 Buchhave, L. A., Latham, D. W., Johansen, A., et al. 2012, *Natur*, 486, 375
 Choi, J., Dotter, A., Conroy, C., et al. 2016, *ApJ*, 823, 102
 Ciardi, D. R., Beichman, C. A., Horch, E. P., & Howell, S. B. 2015, *ApJ*, 805, 16
 Claret, A. 2018, *A&A*, 618, A20
 Coelho, P., Barbuy, B., Meléndez, J., Schiavon, R. P., & Castilho, B. V. 2005, *A&A*, 443, 735
 Donati, J. F., Moutou, C., Malo, L., et al. 2016, *Natur*, 534, 662
 Dong, S., Xie, J.-W., Zhou, J.-L., Zheng, Z., & Luo, A. 2018, *PNAS*, 115, 266
 Dotter, A. 2016, *ApJS*, 222, 8
 Duffell, P. C., & Chiang, E. 2015, *ApJ*, 812, 94
 Eastman, J. 2017, EXOFASTv2, Astrophysics Source Code Library, ascl:1710.003
 Eastman, J., Gaudi, B. S., & Agol, E. 2013, *PASP*, 125, 83
 Fűrész, G., Szentgyorgyi, A. H., & Meibom, S. 2008, in *Precision Spectroscopy in Astrophysics*, Proc. ESO/Lisbon/Aveiro Conf., ed. N. C. Santos (Heidelberg: Springer), 287
 Foreman-Mackey, D., Agola, E., Ambikasaran, S., & Angus, R. 2017, *AJ*, 154, 220
 Foreman-Mackey, D., Hogg, D. W., Lang, D., & Goodman, J. 2013, *PASP*, 125, 306
 Fulton, B. J., & Petigura, E. A. 2018, *AJ*, 156, 264
 Furlan, E., Ciardi, D. R., Everett, M. E., et al. 2017, *AJ*, 153, 71
 Gaudi, B. S., Stassun, K. G., Collins, K. A., et al. 2017, *Natur*, 546, 514
 Gaudi, B. S., & Winn, J. N. 2007, *ApJ*, 655, 550
 Grunblatt, S. K., Huber, D., Gaidos, E., et al. 2017, *AJ*, 154, 254
 Günther, M. N., Queloz, D., Gillen, E., et al. 2017, *MNRAS*, 472, 295
 Günther, M. N., Queloz, D., Gillen, E., et al. 2018, *MNRAS*, 478, 4720
 Høg, E., Fabricius, C., Makarov, V. V., et al. 2000, *A&A*, 355, L27
 Holden, F. 1978, *PASP*, 90, 587
 Horch, E., van Altena, W. F., Girard, T. M., et al. 2001, *AJ*, 121, 1597
 Huang, C., Wu, Y., & TriAUD, A. H. M. J. 2016, *ApJ*, 825, 98
 Huang, C. X., Shporer, A., Dragomir, D., et al. 2018, arXiv:1807.11129
 Huber, D., Zinn, J., Bojsen-Hansen, M., et al. 2017, *ApJ*, 844, 102
 Jensen, A. G., Cauley, P. W., Redfield, S., Cochran, W. D., & Endl, M. 2018, *AJ*, 156, 154
 Johnson, J. A., Fischer, D. A., Marcy, G. W., et al. 2007, *ApJ*, 665, 785
 Jones, M. I., Brahm, R., Espinoza, N., et al. 2018, *A&A*, 613, A76
 Jones, M. I., Brahm, R., Wittenmyer, R. A., et al. 2018, *A&A*, 602, A58
 Jones, M. I., Jenkins, J. S., Rojo, P., & Melo, C. H. F. 2011, *A&A*, 536, A71
 Kempton, E. M.-R., Bean, J. L., Louie, D. R., et al. 2018, *PASP*, 130, 114401
 Knutson, H. A., Fulton, B. J., Montet, B. T., et al. 2014, *ApJ*, 785, 126
 Kreidberg, L., Bean, J. L., Désert, J.-M., et al. 2014, *ApJL*, 793, L27
 Kurucz, R. 1993, ATLAS9 Stellar Atmosphere Programs and 2 km/s grid. Kurucz CD-ROM No. 13 (Cambridge: Smithsonian Astrophysical Observatory), 13
 Lai, D. 2016, *AJ*, 152, 215
 Laughlin, G., Crismani, M., & Adams, F. C. 2011, *ApJL*, 729, L7
 Lee, E. J., & Chiang, E. 2016, *ApJ*, 817, 90

- Lin, D. N. C., Bodenheimer, P., & Richardson, D. C. 1996, *Natur*, **380**, 606
- Lopez, E. D., & Fortney, J. J. 2016, *ApJ*, **818**, 4
- Mayor, M., Pepe, F., Queoz, D., et al. 2003, *Msngr*, **114**, 20
- Niraula, P., Redfield, S., Dai, F., et al. 2017, *AJ*, **154**, 266
- Petigura, E. A. 2015, PhD thesis, Univ. California, Berkeley
- Petrovich, C. 2015, *ApJ*, **805**, 75
- Rasio, F. A., & Ford, E. B. 1996, *Sci*, **274**, 954
- Ricker, G. R., Winn, J. N., Vanderspek, R., et al. 2015, *JATIS*, **1**, 014003
- Robin, A. C., Reylé, C., Derrière, S., & Picaud, S. 2003, *A&A*, **409**, 523
- Roeser, S., Demleitner, M., & Schilbach, E. 2010, *AJ*, **139**, 2440
- Rossum, G. 1995, Python Reference Manual (Amsterdam: CWI)
- Santerne, A., Díaz, R. F., Almenare, J.-M., et al. 2015, *MNRAS*, **451**, 2337
- Schlafly, E. F., & Finkbeiner, D. P. 2011, *ApJ*, **737**, 103
- Schlaufman, K. C., & Winn, J. N. 2013, *ApJ*, **772**, 143
- Shporer, A., O'Rourke, J. G., Knutson, H. A., et al. 2014, *ApJ*, **788**, 92
- Siverd, R. J., Brown, T. M., Hygelund, J., et al. 2016, *Proc. SPIE*, **9908**, 99086X
- Siverd, R. J., Brown, T. M., Stuart, B., et al. 2018, *Proc. SPIE*, **10702**, 107026C
- Snedden, C. 1973, *ApJ*, **184**, 839
- Sousa, S. G., Santos, N. C., Adibekyan, V., Delgado-Mena, E., & Israelian, G. 2015, *A&A*, **577**, A67
- Stassun, K. G., Oelkers, R. J., Pepper, J., et al. 2018, *AJ*, **156**, 102
- Stephan, A. P., Naoz, S., & Gaudi, B. S. 2018, *AJ*, **156**, 128
- Stevenson, K. B., Bean, J. L., Seifahrt, A., et al. 2014, *AJ*, **147**, 161
- Sullivan, P. W., Winn, J. N., Berta-Thompson, Z. K., et al. 2015, *ApJ*, **809**, 77
- Tokovinin, A., Fischer, D. A., Bonati, M., et al. 2013, *PASP*, **125**, 1336
- van der Walt, S., Colbert, S. C., & Varoquaux, G. 2011, *CSE*, **13**, 22
- Van Eylen, V., Albrecht, S., Gandolfi, D., et al. 2016, *AJ*, **152**, 143
- Villaver, E., & Livio, M. 2009, *ApJL*, **705**, L81
- Vogt, S. S., Allen, S. L., Bigelow, B. C., et al. 1994, *Proc. SPIE*, **2198**, 362
- Wang, S., Addison, B., Fischer, D. A., et al. 2018, *AJ*, **155**, 70
- Winn, J. N., Fabrycky, D., Albrecht, S., & Johnson, J. A. 2010, *ApJL*, **718**, L145
- Winn, J. N., Noyes, R. W., Holman, M. J., et al. 2005, *ApJ*, **631**, 1215
- Winn, J. N., Sanchis-Ojeda, R., & Rappaport, S. 2018, arXiv:1803.03303
- Wu, Y., & Lithwick, Y. 2011, *ApJ*, **735**, 109
- Wu, Y., Murray, N. W., & Ramsahai, J. M. 2007, *ApJ*, **670**, 820
- Zechmeister, M., Reiners, A., Amado, P. J., et al. 2018, *A&A*, **609**, A12
- Zucker, S., & Mazeh, T. 1994, *ApJ*, **420**, 806